Lidar Measurements of Polar Stratospheric Clouds in the Arctic

Peggy Achtert

Cover image: Radar Hill Station at Esrange Space Center.
Photo by: Peggy Achtert.

ISBN 978-91-7447-657-6

Printed in Sweden by US-AB, Stockholm 2013

Distributor: Department of Meteorology, Stockholm University

List of Papers

The following papers, referred to in the text by their Roman numerals, are included in this thesis.

PAPER I: **Pure rotational-Raman channels of the Esrange lidar for temperature and particle extinction measurements in the troposphere and lower stratosphere**
P. Achtert, M. Khaplanov, F. Khosrawi, and J. Gumbel, *Atmos. Meas. Tech.*, **6**, 2013, DOI: 10.5194/amt-6-91-2013.

PAPER II: **Assessing lidar-based classification schemes for Polar Stratospheric Clouds based on 16 years of lidar measurements at Esrange, Sweden**
P. Achtert and M. Tesche, *J. Geophys. Res.*, **submitted**, 2013, DOI: 2013JD019631

PAPER III: **On the linkage between tropospheric and Polar Stratospheric clouds in the Arctic as observed by space–borne lidar**
P. Achtert, M. Karlsson Andersson, F. Khosrawi, and J. Gumbel, *Atmos. Chem. Phys.*, **12**, 2012, DOI: 10.5194/acp-12-3791-2012.

PAPER IV: **Investigation of polar stratospheric clouds in January 2008 by means of ground-based and space–borne lidar measurements and microphysical box model simulations**
P. Achtert, F. Khosrawi, U. Blum, and K. H. Fricke, *J. Geophys. Res.*, **116**, 2011, DOI: 10.1029/2010JD014803.

Author's contribution

I made the following contributions to the papers presented in this thesis. The idea for the improved setup of the Esrange lidar originated from K. H. Fricke, the developer of the lidar system at Esrange, northern Sweden. The design for the experimental setup of the temperature channels was developed by M. Khaplanov, K. H. Fricke, and myself. I did most of the writing for Paper I. The idea for Paper II originated from a discussion between M. Tesche and myself. I am responsible for most of the data analysis and we did the writing together in equal parts. The idea for Paper III resulted from discussions between L. Petrykowska, F. Khosrawi, H. Körnich, and myself. The analysis for paper III was done together with M. Karlsson Andersson as part of her bachelor thesis. I did most of the writing. In Paper IV, I analyzed the lidar data and did most of the writing. The model simulations were done by F. Khosrawi.

Papers not included in this thesis:

Denitrification and polar stratospheric cloud formation during the Arctic winter 2009/2010

F. Khosrawi, J. Urban, M. C. Pitts, P. Voelger, P. Achtert, M. Kaphlanov, M. L. Santee, G. L. Manney, D. Murtagh, and K. H. Fricke, *Atmos. Chem. Phys.*, **11**, 2011, DOI: 10.5194/acp-11-8471-2011.

A novel rocket-based in-situ collection technique for mesospheric and stratospheric aerosol particles

W. Reid, P. Achtert, N. Ivchenko, P. Magnusson, T. Kuremyr, V. Shepenkov, and G. Tibert, *Atmos. Meas. Tech.*, **6**, 2013, DOI: 10.5194/amt-2013-216.

Contents

1. Introduction

Polar Stratospheric Clouds (PSCs) have been observed since the early 1870s at northern high latitudes and the late 1890s at southern high latitudes (Hallett & Lewis, 1967; Stanford & Davis, 1974). In the southern hemisphere a larger number of PSC sightings has been reported compared to the northern hemisphere. The formation of PSCs strongly depends on temperature. The undisturbed evolution of the polar vortex in the southern hemisphere allows for a development of colder temperatures compared to the northern hemisphere. Colder temperatures in turn form the foundation for widespread and long–lasting PSC occurrence, and hence, observations. The first studies that describe the spatial and temporal occurrence of PSCs over Antarctica were conducted by McCormick *et al.* (1982) and Steele *et al.* (1983) and relied on satellite measurements. Further, Steele *et al.* (1983) showed that PSCs seemed to consist of almost pure water ice particles formed by condensation of water vapor on preexisting background aerosol. These findings were in agreement with temperatures around the frost point of water that have been observed in connection to PSC events.

However, the biggest improvement in the understanding of PSC-related processes was obtained from active (height–resolved) optical remote measurements with lidar. Lidar instruments can be operated from the ground, from an aircraft, or from space. Ground–based lidar measurements can provide continuous observations with high temporal and vertical resolution but are limited to a certain location. Space–based lidar measurements provide measurements with a high vertical and spatial resolution, but have a low observation rate at a given location due to the orbital constrains of polar–orbiting satellites. It is a combination of ground–based and space–borne lidar measurements that provides a unique possibility to investigate the formation and alteration of clouds and aerosol layers in both space and time.

Most studies of PSCs — especially long time series — are based on measurements of their optical properties with lidar. The classification of PSCs is based on their scattering properties as seen by lidar. Poole & McCormick (1988) presented the first lidar-based classification of Arctic PSCs. The authors could separate two types of PSC from the lidar measurements: type I was found to consist of liquid droplets and type II was found to be made of frozen water ice particles. Later studies with more sensitive instruments re-

vealed an additional type of PSC type. Consequently, type I was split into two subclasses that showed optical properties typical for non-spherical (solid) particles (type Ia) and spherical (liquid) particles (type Ib), respectively.

Note that the mechanisms for the formation of type Ia PSCs are still unclear — as are the interactions and relations between the different constituents of PSCs that are often observed simultaneously. These uncertainties regarding our understanding of PSC formation and existence also need to be considered in connection with climate change. The systematic cooling of the stratosphere that is induced by increasing concentrations of greenhouse gases could favor the formation of PSCs. An increase in the number and area of PSCs could, in turn, affect the stratospheric ozone layer.

There is a variety of open questions regarding our understanding of PSCs: (1) What is the occurrence frequency of different PSC types? (2) What controls the formation of different PSC types and subtypes? (3) How representative are stationary PSC observations for a wider region? (4) How do the different PSC constituents interact? (5) Is the formation obtained from lidar measurements sufficient for a comprehensive understanding of the chemical properties of PSCs and the processes that they are associated with? (6) Are PSC observations from different platforms and instrument comparable? (7) Which informations would be needed to improve the understanding of PSCs?

The purpose of this work was to shed some light on these topics. This thesis focuses on PSC observation conducted with the Esrange lidar and the polar–orbiting space–borne CALIPSO lidar. PSCs and their connection to ozone depletion will be discussed in Chapter 2. The Esrange lidar is a multi–wavelength lidar that operates since 1997 at Esrange (68° N, 21° E) in northern Sweden, about 150 km north of the Arctic circle. Within the framework of this thesis improvement have been made to the lidar system. These improvements will be discussed in Chapter 3. The space–borne lidar will be briefly introduced in Chapter 4. Chapter 3 and 4 also gives an overview of the investigations of Arctic PSCs that were carried out in the framework of this thesis.

2. Polar Stratospheric Clouds and Related Processes

During late winter and early spring PSCs provide the surface for heterogeneous reactions which transform stable chlorine and bromine species into their highly reactive ozone–destroying states. Therefore, PSCs are important for ozone depletion during late winter and early spring at high latitudes. The type of PSC as well as their temporal and spatial extent are important for the occurrence of heterogeneous reactions and ozone depletion in the polar stratosphere. But what are PSCs?

2.1 Polar Stratospheric Clouds

When we consider observations and classifications of clouds, our imagination and experience is usually restricted to the lowermost layer of the atmosphere — the troposphere which extends from the surface to about 10 km height. The troposphere is that layer of the atmosphere in which meteorological processes — commonly called weather — are observable and recognizable the best way. However, the occurrence of clouds is not restricted to the troposphere. Since the first publication of a "cloud atlas" by Hildebrandson *et al.* (1896) in 1896 PSCs were considered as being clouds. Despite their appearance which differs strongly from regular clouds, nobody imagined these clouds to be completely different from their tropospheric counterparts.

The recording of observations of PSCs started in 1893 when Henrik Mohn published his collected data of iridescent clouds over southern Sweden. His recordings vary between simple notes of the presence of a cloud and pictures. He referred to PSCs as Mother–of–Pearl–Cloud because of their brilliant iridescence (Mohn, 1893). However, he did not determine the height of the clouds that were documented by means of photographs. What he did instead was to show a correlation between the occurrence of iridescent clouds and the synoptic situation. He figured that PSCs are a phenomena that usually occurs during winter, downwind of the Norwegian mountains, and to the south of deep eastward–moving low–pressure system. Drawing this conclusion he was one of the first persons to recognize that PSCs are a phenomena that is typical for

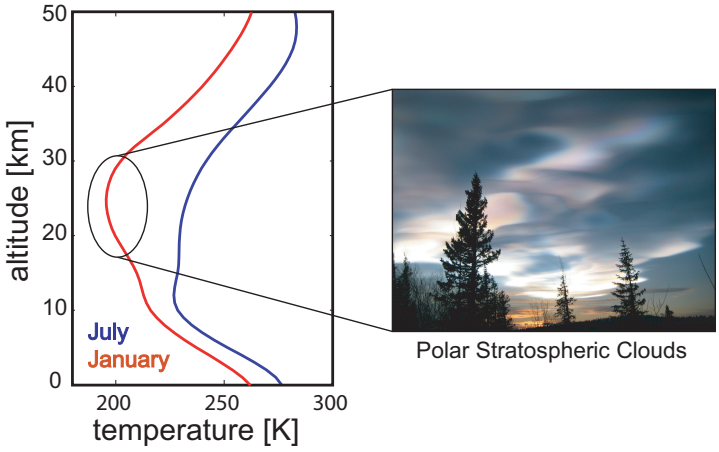

Figure 2.1: Climatological mean temperatures above Esrange (68° N, 21° E) for January (red) and July (blue). The temperature profiles were retrieved from the MSIS-E-90 Atmosphere Model. PSCs can form at temperature below 195 K between 15 and 28 km height.

Scandinavian winters. PSCs are best visible during sunrise and sunset when they are illuminated by the sun from below the horizon.

Störmer (1929, 1931) was the first to determine the height of PSCs by applying triangulation to photographs. He concluded that PSCs occur in the stratosphere at an altitude between 22 and 27 km. The stratosphere is the atmospheric layer that connects to the troposphere and extends up to 50 km height. In the troposphere the temperature decreases with height. The stratosphere on the other hand is distinguished by a reversal of the temperature gradient, which is due to absorption of ultraviolet (UV) radiation by ozone. The absorption of harmful UV radiation (from about 200 nm to 315 nm wavelength) enables live on Earth as we know. Eighty-five to ninety percent of the atmospheric ozone is found in the stratosphere. The atmospheric ozone layer (height–region of the highest ozone concentration) is located in the stratosphere between 10 and 35 km height. The maximum of the ozone concentration is located in the lower stratosphere. A temperature maximum marks the upper limit of the stratosphere, about 50 km above the Earth's surface.

Figure 2.1 shows the average temperature profile for January (red) and July (blue) above Esrange. In summer the stratospheric temperature is higher than in winter due to higher absorption rate of UV radiation. The average temperature profile for January shows a negative temperature gradient in the stratosphere which leads to a less pronounced tropopause. The tropopause is a height region of constant temperature (vertical temperature gradient of

zero) between the troposphere and the stratosphere. The negative temperature gradient in the winter stratosphere is lower than within the troposphere.

PSCs can be formed in the stratosphere between 15 and 28 km height when the temperature is below 195 K. The extremely low temperatures that are necessary for PSC formation can only be reached inside of the polar vortex. This stable and cold vortex dominates the stratospheric circulation during winter months. The formation of different PSC types depends strongly on temperature. PSCs of type Ia and Ib occur at temperatures below 195 K. Type Ia consist of nitric acid di- or trihydrate crystals (NAD or NAT). Type Ib include supercooled liquid ternary solutions (STS) that consist of H_2SO_4, HNO_3, and H_2O. PSCs of type II are formed below the ice–frost point and consist of pure water ice particles (e.g. Browell *et al.* (1990); Carslaw *et al.* (1994); Toon *et al.* (1990); Voigt *et al.* (2005)).

In the Arctic stratosphere the formation temperature of PSCs — in particular that of type II PSCs, which are strongly related to the altitude–dependent ice frost point — is rarely attained synoptically. Previous studies (Carslaw *et al.*, 1998; Dörnbrack *et al.*, 2000; Höpfner *et al.*, 2001; Juárez *et al.*, 2009) concluded that Arctic PSCs are mostly formed due to gravity–wave–induced temperature modifications. Recent studies showed that gravity–wave–induced temperature modifications are also important for Antarctic PSC formation in early winter when synoptic processes are not sufficient for producing the temperatures necessary for PSC formation (Höpfner *et al.*, 2006; McDonald *et al.*, 2009). Carslaw *et al.* (1998) and Teitelbaum *et al.* (2001) showed that local cooling in the lower stratosphere can be caused by meso–to synoptic–scale events in the troposphere (e.g. low–pressure system). This diabatic cooling effect can affect both PSC formation and their microphysical properties, i.e., PSC type (Adhikari *et al.*, 2010). Furthermore, Wang *et al.* (2008) showed that during the period June–October 2006 66% and 52% of the PSCs over western and eastern Antarctica, respectively, were associated with an underlying deep-tropospheric cloud systems.

2.2 The Polar Vortex

In the stratosphere a wave–driven meridional circulation is transporting air from the tropics to high latitudes where it subsides. This large scale circulation is known as Brewer–Dobson circulation. During the polar night (no solar heating, no absorption of UV radiation by ozone) the air cools, descends, and a strong westerly jet develops in the stratosphere and forms the polar vortex. The polar vortex forms in the fall, reaches maximum strength in mid–winter, and decays in late winter to early spring. The westerly winds of the vortex allow for a vertical propagation of quasi–stationary planetary waves into the

stratosphere. Inside the polar vortex air is isolated and radiative cooled. Atmospheric waves (e.g., gravity waves, planetary waves) have different effects on the temperature profile in the stratosphere. Gravity waves are excited in the troposphere, e.g. air flow over mountains, frontal systems or convection. Planetary waves (forced Rossby waves) are excited by large–scale topography or by land–sea temperature contrast. The input of energy from breaking waves into the upper stratosphere during polar winter triggers subsidence of air masses and thus, to a warming in the stratosphere (Holton, 1992). Stratospheric warmings are defined by a temperature increase of at least 10 K within a few days together with a reversal of the zonal wind and the temperature gradient between the pole and 60°N. Depending of their strength and progression four different types of stratospheric warming are defined (Labitzke & Loon, 1999):

- Canadian Warming: Warming occurs in the beginning of winter. An area of warm air develops over Canada and moves along the edge of the vortex to the north pole.

- Minor Warming: Appears regularly during winter and is defined by a temperature increase of more than 25 K over a period of no longer than one week.

- Major Warming: Is marked by a temperature increase and a temperature-gradient reversal at the 30–hPa level or below together with a reversal of the zonal wind from easterly to westerly directions. A major warming leads to a breakup of the polar vortex, and thus, allow for a mixing of polar air masses with the ones at polar mid-latitudes.

- Final Major Warming: Occurs at the end of the season and the polar vortex does not recover.

Topographically forced planetary waves are much stronger in the northern hemisphere compared to the southern hemisphere. This effect leads to higher occurrence rate of minor and major stratospheric warmings in the northern hemisphere.

2.3 Stratospheric Ozone

Stratospheric chemistry is centered around ozone. Most other gases entering the stratosphere are long-living and originate in the troposphere (e.g., nitrous oxide (N_2O), methane (CH_4), chlorofluorocarbons (CFCs)) or are inject into

the stratosphere by volcanic eruptions. Therefore, inorganic compounds dominate the composition of the stratosphere: nitrogen oxides, nitric acid, sulfuric acid, ozone, halogens, and halogen oxides from the destruction of CFCs.

Stratospheric ozone is mainly created in the tropical stratosphere by photolysis of oxygen. The formation and destruction of ozone is described by the Chapman cycle (Seinfeld & Pandis, 2006):

1. Formation through photolysis of oxygen by short-wave UV radiation ($\lambda \leq 242$ nm)
   $O_2 \xrightarrow{h\nu} O + O$

2. With a help of a catalyst, molecular and atomic oxygen form ozone
   $O + O_2 + M \rightarrow O_3 + M$

3. Photodissociation of O_3 breaks down ozone into atomic and molecular oxygen ($\lambda \leq 366$ nm)
   $O_3 \xrightarrow{h\nu} O + O_2$

4. and ozone is destroyed through the reaction with atomic oxygen
   $O_3 + O(^1D) \rightarrow O_2 + O_2$

Stratospheric ozone can also be destroyed through catalytic reactions:

- $X + O_3 \rightarrow OX + O_2$
  $OX \rightarrow X + O_2$
  With the net result:
  $O_3 + O \rightarrow O_2 + O_2$

Catalysts X for the destruction process can be chlorine (Cl), hydrogen (H), nitric oxide (NO), or hydroxyl (OH). This process continues as long the catalyst is not used up by other reactions in the stratosphere (e.g. Crutzen (1979)). A great amount of NO and Cl is of anthropogenic origin and is formed through photolysis of CFCs. On average one Cl can destroy hundreds of ozone molecules before it is removed from the stratosphere. However, Cl can be temporarily removed from the catalytic cycle and be stored in stable reservoir species. The most important reservoir species is chlorine nitrate ($ClON0_2$).

During late winter and early spring PSCs provide the surface for heterogeneous reactions that transform stable chlorine and bromine species into highly reactive ozone–destroying states. Therefore PSCs are important for high–latitude ozone depletion.

The heterogeneous chemistry that is responsible for ozone depletion can be described by the following processes (Seinfeld & Pandis, 2006):

1. Activation of chlorine on cloud particles in PSCs of type Ia
   $ClONO_2 + HCl \rightarrow Cl_2 + HNO_3$

2. Indirect activation of chlorine on cloud particles in PSCs of type Ib
   $ClONO_2 + H_2O \rightarrow HOCl + HNO_3$
   $HOCl + HCl \rightarrow Cl_2 + H_2O$

3. Photolysis of Cl_2
   $Cl_2 \xrightarrow{h\nu} Cl + Cl$

4. Ozone destruction
   $2(Cl + O_3 \rightarrow ClO + O_2)$
   $ClO + ClO + M \rightarrow Cl_2O_2 + M$
   $Cl_2O_2 \xrightarrow{h\nu} 2Cl + O_2$
   With the net result:
   $2O_3 \rightarrow 3O_2$

On the surface of PSC particles a heterogeneous chemical process (processes 1 and 2) can occur and activate chlorine to Cl_2. This process occurs during polar winter when sunlight is ascent. Therefore, the lifetime of Cl_2 in the polar vortex is very long during polar night. It lasts until sunlight is available at higher latitudes. As soon as the sun returns in spring process 3 can start and Cl_2 is split into two Cl. The latter start ozone destruction (process 4) by producing ClO. The concentration of ClO during process 4 is stable. The only way to reduce the ClO concentration is by chlorine deactivation:

$$HNO_3 \xrightarrow{h\nu} NO_2 + OH$$
$$ClO + NO_2 + M \rightarrow ClONO_2 + M$$

However, this process is not working very well in the southern polar vortex. The reason for that is that compared to the northern polar vortex the southern polar vortex is much more stable and the formation temperature for PSCs of type Ia and II is reached more often. Under these conditions HNO_3 cloud particles can form. If these cloud particles get large enough they start to sediment and can be removed from the stratosphere. The latter is known as denitrification. As a consequence of the fading availability chlorine deactivation is slowed down or stops completely. In that case, chlorine is binded into the reservoir species favorable conditions for ozone destruction by ClO are created (Seinfeld & Pandis, 2006).

3. Esrange Lidar Measurements and Findings

Lidar (light detection and ranging) is an active remote–sensing instrument for range–resolved measurements in the atmosphere and oceans. It allows for measurements of a variety of atmospheric parameters such as temperature, wind, trace gases, aerosols, and clouds with high spatial and temporal resolution. Further, it allows for observations under ambient conditions. Lidar measurements can cover a height range between the ground and 120 km altitude. Over the last 30 years lidar helped to monitor the evolution of volcanic aerosols layers in the stratosphere, stratospheric ozone depletion, and to investigate the role of PSCs in ozone depletion.

3.1 Setup of the Esrange Lidar

The Department of Meteorology of the Stockholm University operates the Esrange lidar at Esrange Space Center (68° N, 21° E) near the Swedish city of Kiruna. It was originally installed in 1997 by the University of Bonn. A predecessor of the lidar system was installed at the Andøya Rocket Range in northern Norway. Measurements with the Esrange lidar cover the atmosphere from about 4 to 90 km altitude. It can provide upper tropospheric, stratospheric, and mesospheric measurements of clouds and aerosol layers as well as atmospheric temperature profiles (Blum & Fricke, 2005a). Further, polarization-sensitive measurements allow for a discrimination between aerosols, cloud droplets, ice crystals, and PSC constituents in the upper troposphere and stratosphere. The simultaneously derived temperature profiles can be used for studies of atmospheric gravity waves.

In principle, a lidar system consists of a transmitter unit and a receiver unit. The latter comprises an optical detector for the detailed analysis of the measured signal. A laser is used to generate light pulses with specific spectral properties (Wandinger (2005) and references therein). The Esrange lidar uses a pulsed Nd:YAG solid-state laser with a repetition rate of 20 Hz.

The setup of the transmitter unit of the Esrange lidar is shown in Figure 3.1. The primary wavelength of the Nd:YAG laser is 1064 nm. Until 2013 only the

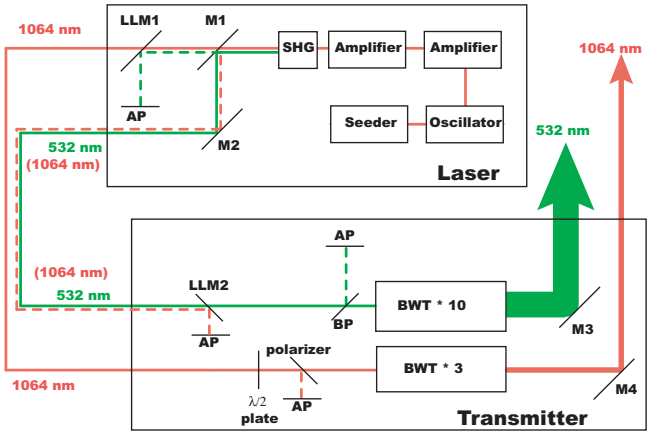

Figure 3.1: Optical setup of the transmitter unit of the Esrange lidar. The Nd:YAG laser emits light at 1064 nm which is frequency–doubled to 532 nm by a means of a second harmonic generator (SHG). The mirrors M1 and M2 separate light at 532 nm from that at 1064 nm and guide the beams out of the laser housing. Laser–line mirrors (LLM) separate the remaining unwanted light at 532 and 1064 nm to a absorber plates (AP). A Brewster plate (BP at 532 nm) and a sheet polarizer (at 1064 nm) are used to assure that only purely linearly polarized light is emitted. Beam widening telescopes (BWT) expand the beams before steerable mirrors (M3, M4) direct the beam to the atmosphere. The figure was adapted from (Blum & Fricke, 2005a).

frequency–doubled light (532 nm) was used for measurements with the Esrange lidar. In January 2013, the system was upgraded to also allow for measurements at 1064 nm. Adding another wavelength to the measurement setup allows for a more detailed characterization of aerosols and PSCs. Note that spectral optical properties are strongly connected to the size of the scatterers. A beam expander within the transmitter is used to reduce the divergence of the beam before it is send out into the atmosphere. Reducing the beam divergence enables the use of a small field of view in the receiver, and thus, helps to reduce the solar background from the measured signal of backscattered light.

The receiver unit of the Esrange lidar consists of an assembly of three identical Newtonian telescopes with individual mirror diameters of 50.8 cm and focal lengths of 254 cm. For each telescope backscattered light is collected into one so–called focal box. There, light is separated according to wavelength and state of polarization. The backscattered light incorporates elastic backscatter by molecules, aerosols, and clouds at the wavelength of the emitted laser light

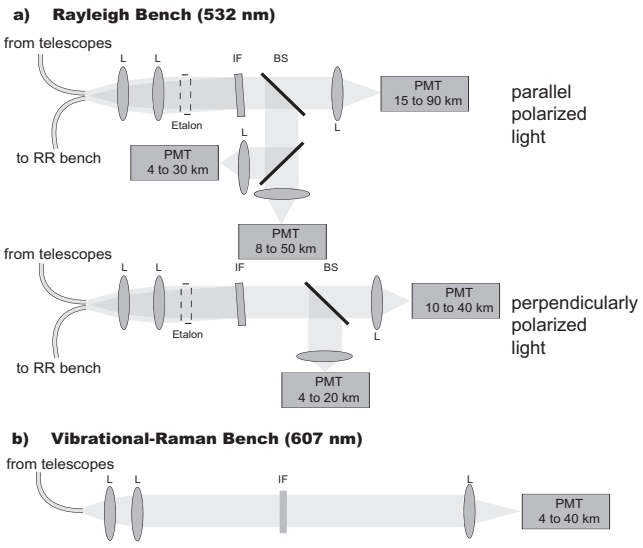

Figure 3.2: Schematic setup of the optical benches installed in 1997. (a) Setup of the Rayleigh bench. (b) Setup of the vibrational–Raman bench. IF: interference filter, L: lens, BS: beam splitter, PMT: photomultiplier tube, RR: rotational–Raman. Etalons are used to weaken the contribution of sunlight to the measured signal during daytime measurements. Numbers in the boxes mark the measurement range of the individual channels.

and inelastic (frequency–shifted) backscatter by molecules. Optical fibers are used to guide the light from the individual branches of the focal boxes to the detector. The use of three individual telescopes increases the flexibility of the lidar. In standard configuration, identical focal boxes are used for all three telescopes. In this way, the total signal is maximized and allows for measurements up to 90 km height. Depending on the aim of the measurement, it is also possible to attach differently optimized focal boxes wavelengths to the individual telescopes.

The Esrange lidar system has in total four optical detector benches (Figures 3.2 and 3.3):

- **Rayleigh bench** (Figure 3.2a) for measurements of elastic backscatter by cloud and aerosol layers in the upper troposphere, stratosphere, and mesosphere at 532 nm. Polarization sensitive measurements (parallel and perpendicularly backscattered light with respect to the plane of polarization of the emitted laser light) allow for a discrimination of spherical and non–spherical scatterers (i.e., aerosol particles, cloud droplets, and ice crystals). The signal detected in the Rayleigh channel is also

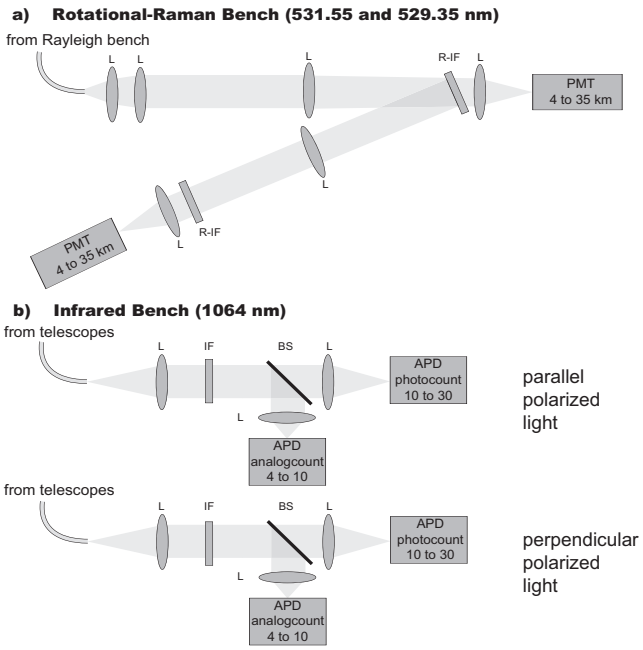

Figure 3.3: Schematic setup of the new optical benches installed in 2010 and 2013. (a) Setup of the rotational–Raman bench. The signal for the rotational–Raman bench comes from the Rayleigh bench (Figure 3.2a). The pick–up is based on light that is reflected by the interference filters in the Rayleigh bench. (b) Setup of the infrared bench. IF: interference filter, L: lenses, BS: beam splitter, PMT: photomultiplier tube, APD: avalanche photodiode.

used to obtain temperature profiles in the aerosol–free atmosphere between 30 and 90 km height. The optical bench is designed in a cascade structure to cover a large dynamical range of 7 to 8 (parallel channel) and from 6 to 7 orders (perpendicular channel) of magnitude. This translate into a coverage of heights of up to 90 and 40 km, respectively. The individual PMTs are protected against high photo counts from lower atmospheric layers by means of chopper.

- **Vibrational–Raman bench** (Figure 3.2b) for measurements of inelastic backscatter by molecular nitrogen at 607 nm. The signal of this channel is used to obtain a profile of the molecular backscatter coefficient.

- **Rotational–Raman bench** (Figure 3.3a) for measurements of inelastic backscatter by molecular nitrogen and oxygen at 531.7 and 529.35 nm. The signals of these channels are used to obtain temperature profiles in the upper troposphere and lower stratosphere. The rotational–Raman

bench was installed in November 2010 (Paper I).

- **Infrared bench** (Figure 3.3b) for measurements of elastic backscatter at 1064 nm. The signal is used for detailed aerosol characterization in the upper troposphere and lower stratosphere. The infrared bench was installed in January 2013.

3.2 Measurements of Clouds and Aerosol Layers

The backscattered light at 532 nm is detected in two orthogonal planes of polarization for detailed measurements of clouds and aerosol layers. Light with the same plane of polarization as the emitted laser light is referred to as parallel polarized or co–polarized (superscript $\parallel$) and light with a polarization plane perpendicular to the one of the emitted laser light is called perpendicularly polarized or cross–polarized (superscript $\perp$).

Measurements of backscattered light in the parallel and perpendicular channels are used to derive the parallel and perpendicular backscatter ratios ($R^{\parallel}$ and $R^{\perp}$, respectively), the aerosol backscatter coefficient (β_{aer}), and the linear aerosol depolarization ratio (δ_{aer}). The general definition of the backscatter ratio is

$$R = \frac{\beta}{\beta_{\text{mol}}} = \frac{\beta_{\text{aer}} + \beta_{\text{mol}}}{\beta_{\text{mol}}}, \tag{3.1}$$

where the total volume backscatter coefficient β represents the sum of the aerosol backscatter coefficient β_{aer} and the molecular backscatter coefficient β_{mol}. The backscatter ratio can also be calculated individually from the measurements in the polarized channels as

$$R^{\parallel} = \frac{\beta^{\parallel}_{\text{aer}} + \beta^{\parallel}_{\text{mol}}}{\beta^{\parallel}_{\text{mol}}} \tag{3.2}$$

and

$$R^{\perp} = \frac{\beta^{\perp}_{\text{aer}} + \beta^{\perp}_{\text{mol}}}{\beta^{\perp}_{\text{mol}}}. \tag{3.3}$$

The linear aerosol depolarization ratio is derived from the measurements of cross- and co-polarized signals as

$$\delta_{\text{aer}} = \frac{\beta^{\perp}_{\text{aer}}}{\beta^{\parallel}_{\text{aer}}} = \left(\frac{R^{\perp} - 1}{R^{\parallel} - 1} \right) \delta_{\text{mol}} \tag{3.4}$$

where $\delta_{\text{mol}} = \beta^{\perp}_{\text{mol}} / \beta^{\parallel}_{\text{mol}}$ is the molecular depolarization given as the ratio of perpendicular to parallel molecular backscatter coefficient. In contrast to the

volume depolarization ratio (δ_{vol}) that was used in the first PSC studies, the aerosol depolarization ratio contains no contribution from molecular scattering. It is calibrated according to the method described by Biele *et al.* (2001). The molecular fraction of the received signal of the Rayleigh channel is determined either from the signal above the PSC or by use of a concurrent ECMWF (European Centre for Medium-Range Weather Forecast) temperature and pressure analysis. The molecular signal is normalized to the Rayleigh signal in the aerosol–free part of the atmosphere for the calculation of the backscatter ratios. According to the spectral range of the interference filters in the detector of the Esrange lidar, the value of the molecular depolarization ratio is $\delta_{\mathrm{mol}} = 0.36\ \%$ (Blum & Fricke, 2005a).

3.3 Measurements of Atmospheric Temperature Profiles

Temperature is a key parameter of the state of the atmosphere. Knowledge of atmospheric temperature helps to identify and understand climatological, meteorological, chemical, and dynamical processes.

A variety of techniques can be applied to obtain temperature profiles from lidar measurements. Each of these techniques covers a certain height range as discussed by Behrendt (2005): from the ground to the upper stratosphere (rotational–Raman and high–spectral–resolution lidar), from the upper troposphere and to the lower stratosphere (vibrational–Raman lidar), from the middle stratosphere up to the mesopause (integration technique), and from the mesopause region to the lower thermosphere (resonance–fluorescence technique). Until 2010 the Esrange lidar was only capable of measuring the temperature profile by using the integration technique. The integration technique is applied to the molecular backscatter signal detected in the Rayleigh bench. This signal is proportional to the number density of atmospheric molecules. The temperature can be derived from the number density by the ideal gas law under the assumption that the atmosphere is in hydrostatic equilibrium. The vibrational–Raman technique (Hauchecorne *et al.*, 1992; Keckhut *et al.*, 1990) is a method to extend the temperature retrieval to heights below 30 km. However, detailed information on aerosols, clouds, and ozone concentration is required to obtain temperature profiles with reasonable uncertainty (Faduilhe *et al.*, 2005).

In November 2010 a rotational–Raman bench was added to the Esrange lidar to improve the capabilities for temperature measurements. The new setup is discussed in detailed in Paper I of this thesis. The rotational–Raman technique is based on the fact that the intensity of pure rotational–Raman lines depends on temperature. The ratio of two rotational–Raman signals (λ_1^{RR}, λ_2^{RR}) with opposite temperature dependence allows for temperature measurements

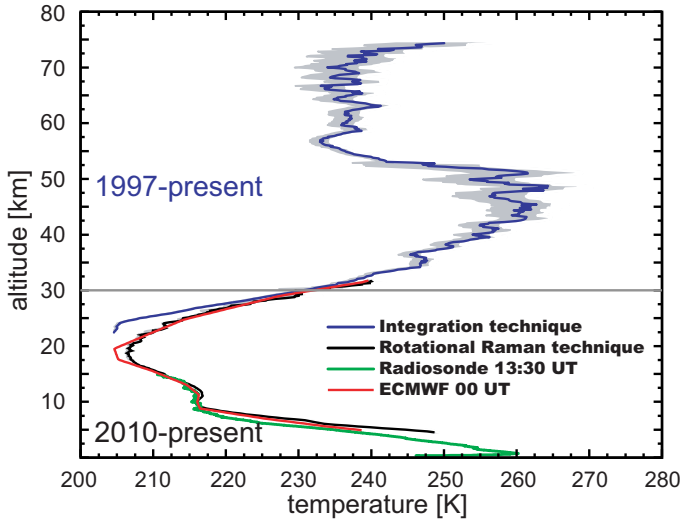

Figure 3.4: Temperature profile between 5 and 75 km height measured between 1339 UT on 14 January 2011 and 0836 UT on 15 January 2011. Profiles were obtained by the integration technique (blue) and the rotational–Raman technique (black). The gray shaded area shows the respective error ranges. For comparison the temperature profiles measured with radiosonde (green) and given by the ECMWF reanalysis (red) are shown as well.

independent of atmospheric transmission (Behrendt, 2005). The rotational–Raman technique in combination with the integration technique can be used to cover an altitude range from 4 km up to 90 km. Temperature measurements from the troposphere to the mesosphere are necessary to understand meteorological processes, like the propagation of gravity waves and the formation of tropospheric and stratospheric clouds.

The rotational–Raman channel of the Esrange lidar was optimized for temperature measurements in the lower Arctic winter stratosphere. The central wavelength (CWL) of the selected interference filters of $\lambda_1^{\mathrm{RR}} = 531.55$ nm and $\lambda_2^{\mathrm{RR}} = 529.35$ nm were chosen to allow for an optimum measurement setup (i.e., minimized measurement uncertainty) for temperatures between 180 K and 200 K. For the chosen temperatures and CWLs the statistical error is less than 0.51 K.

In the new setup (Figure 3.3a) presented in Paper I a reflection from the interference filters in both parallel and perpendicular optical branches of the Rayleigh bench is used to extract rotational–Raman signals from the combined light detected with all three telescopes (Figure 3.2a). The rotational–Raman signals are calibrated to temperature profiles from radiosonde. The calibration

factors obtained from one comparison can be used to retrieve the atmospheric temperature for longer time periods. One example of the combined temperature profile of the new rotational–Raman channel and derived by using the integration technique is shown in Figure 3.4. The temperature profiles were measured on the 14th of January 2011. In the overlap region of the two techniques between 28 to 32 km very good agreement is found. The temperature profiles obtained with the new rotational–Raman channel shows good agreement with both radiosonde and reanalysis output.

3.4 Measurement of PSCs

The earliest lidar measurements of PSCs were conducted from aircraft (Browell *et al.*, 1990; Poole & McCormick, 1988; Toon *et al.*, 1990). From these observations it was found that PSCs show three distinguishable regimes of lidar–derived optical parameters. This led to the conclusion of an existence of three major PSC types (Type Ia, Ib, and II). PSCs of type Ia and Ib occur at temperatures above the ice frost point. Type Ia shows a low parallel backscatter ratio and a high particle depolarization ratio typical for non–spherical particles. Type Ib shows a higher parallel backscatter ratio compared to type Ia and a lower particle depolarization ratio that is typical for spherical particles. It is assumed for PSC studies that spherical scatterers represent liquid particles/droplets and that non–spherical scatterers represent solid particles or ice crystals. David *et al.* (1998) showed that the observed solid particles were never present at temperatures above the temperatures necessary for NAT condensation and that the spherical particles were commonly found at temperatures well below NAT formation temperature (195 K). Figure 3.5 shows two examples of PSC measurements with the Esrange lidar arranged in a $R^{\parallel}$-vs.-$R^{\perp}$ space with additional lines that represent δ_{aer}. The PSC observed on the 8th of January 2012 (Figure 3.5, left) showed two distinct layers of type Ia with an increased perpendicular backscatter ratio (light blue circles) and type Ib with an increased parallel backscatter ratio (light blue circles). A type II PSC was observed on the 27 of January 2011 (Figure 3.5, right). Type II consist of pure water ice and shows a strong increase in both parallel and perpendicular backscatter ratio as well as the linear aerosol depolarization ratio.

From these and earlier lidar observations of PSC optical properties it was inferred that type Ia consists of nitric acid di- or trihydrate crystals (NAD or NAT, respectively) and that type Ib consists of super–cooled liquid ternary solutions (STS). PSCs of type II occur at temperature below the frost point and consist of water ice particles (e.g Carslaw *et al.* (1994); McCormick *et al.* (1982); Poole & McCormick (1988); Voigt *et al.* (2005)). In addition to these three traditional PSC types several sub–types of PSC have been described in

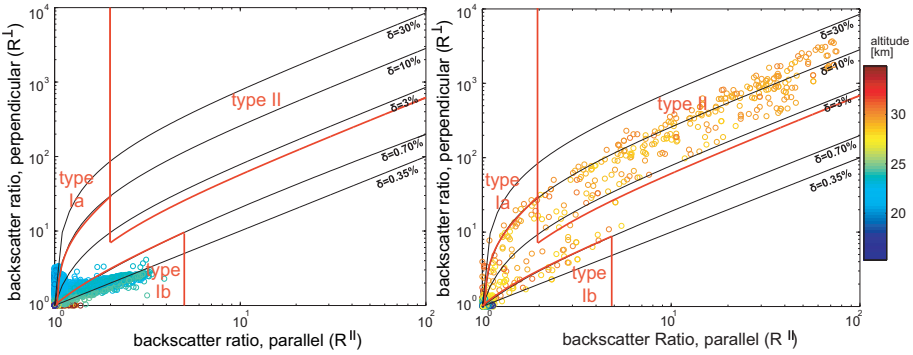

Figure 3.5: PSCs measured with the Esrange lidar on the 8th of January 2012 (left) and on the 27th of January 2011. The colors represent different altitude ranges and the red lines mark the threshold for different PSC types.

the literature. All sub–types, e.g., type Ia enhanced (Tsias *et al.*, 1999), type Ic (Toon *et al.*, 2000), type Id (Stein *et al.*, 1999), or NAT rocks (Fahey *et al.*, 2001) consist of the same constituents as the main types but show different scattering characteristics. All PSCs which cannot be classified clearly by their optical parameters are referred to as mixed–phase clouds (MIX) consisting of a mixture of NAT and STS particles (Biele *et al.*, 2001; Shibata *et al.*, 1999). The thresholds for the different PSC types used for measurements with the Esrange lidar (Blum *et al.*, 2005b) are marked as red lines in Figure 3.5.

Toon *et al.* (2000) defined two main questions regarding the occurrence of different PSC types: (1) What are the statistical frequencies of the different PSC types? and (2) How do sub–classes of type Ia PSCs differ and what mechanisms lead to the formation of one composition rather than another?

Long–term statistics of PSCs occurrence from measurements with ground-based lidar systems over Antarctica (Adriani *et al.*, 2004; Santacesaria *et al.*, 2001) and the Arctic (Blum *et al.*, 2005b; Massoli *et al.*, 2006) were published in the following years. Blum *et al.* (2005b) published a statistical analysis of PSC measurements with the Esrange lidar during the time period 1997–2004. Since then nine more years have been added to the Esrange lidar PSC time series that now covers 17 years or around 542 h of PSC observations. Note that the measurements were conducted on campaign basis during northern–hemispheric winter. Figure 3.6 gives an overview of the observations of PSCs with the Esrange lidar between 1997 and 2013. Most of the campaigns were conducted in January. During the 17 years of lidar measurements there were several winters during which few or no PSC were observed over Esrange. The winters 1998/99, 2001/02, 2003/04, 2008/09, and 2012/13 were embossed by

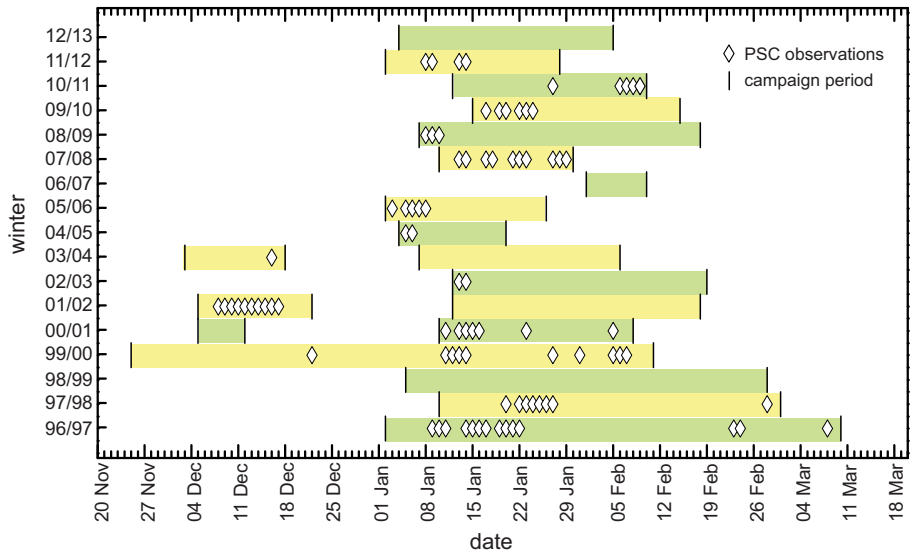

Figure 3.6: Range of measurement campaigns (marked by colored bars) and PSC observations (rectangles) during the time period 1997–2013. The figure was adapted from Blum *et al.* (2005b) and updated.

early major stratospheric warmings.

Figure 3.7 shows the frequency of occurrence of the different PSC types observed during the time period 1997–2004 (Blum *et al.*, 2005b) and for the entire Esrange lidar data set covering the years from 1997 to 2013. The data set contains hourly mean values of the parallel and perpendicularly polarized backscatter ratio and the linear particle depolarization ratio — all measured at 532 nm. The observed PSCs were classified according to the measured values of the their parallel backscatter ratio and the linear particle depolarization ratio. The lowest occurrence frequency is found for PSCs type II (9% between 1997 and 2004 and 6% for the entire period). This is resonable since PSCs of type II are formed at temperatures below the ice–frost point. Such temperatures are rarely reached in the Actic polar vortex. Most of the observations between 1997 and 2013 showed low particle depolarization ratios and low backscatter ratios according to which the observed PSCs were classified as type Ib (47%) or mixtures (33%). The remaining 13% of the observation were classified as type Ia (NAT particles).

The extensive 16-year PSC data set from 1997 to 2012 forms the foundation for an assessment the quality of different PSC classification schemes that is presented in Paper II of this thesis. Lidar–based PSC classification schemes apply standard deliverables of lidar instruments, i.e., the particle backscatter

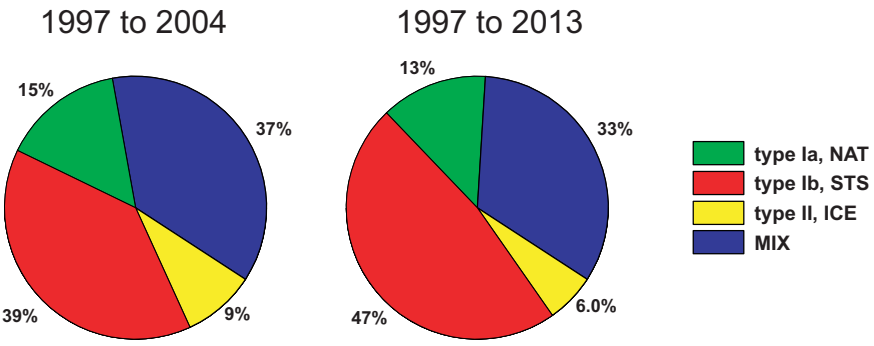

Figure 3.7: Frequency of PSC types observed over Esrange in the time periods from 1997 to 2004 (left, Blum *et al.* (2005b)) and 1997 to 2013 (right, Paper II).

ratio and the particle depolarization ratio. This similarity of input data suggests that the outcome of the different classification schemes should be comparable. Paper II showed that the outcome varies depending on the choice of classification scheme. The discrepancies mainly result from different definitions of PSC type or constituent and their related threshold values of lidar–derived parameters. The inconsistencies of the outcome of different PSC classification schemes impact the understanding of long–term PSC observations documented in the literature. Further, Paper II suggest that an improvement in lidar–based PSC classification might be achieved by using the particle depolarization ratio in combination with polarized (i.e., parallel and perpendicular) rather than total backscatter ratios.

3.5 The Esrange Lidar as Part of the Esrange Research Infrastructure

Since 1997 the Esrange lidar has provided stratospheric and mesospheric measurements of clouds, aerosols and temperatures. In addition to basic scientific studies, the lidar has developed into an important tool to support balloon, aircraft (von Hobe *et al.*, 2012) and rocket campaigns (Gumbel, 2007) based at Esrange. The developments with focus on atmospheric temperatures, volume extinction coefficient measurements, and an improved characterization of clouds and aerosols are important to support future balloon campaigns which aim on studying processes in the troposphere and stratosphere. The new setup of the lidar in combination with the ESRAD (Esrange MST radar) is also a perfect tool for studies of the structure of the high–latitude upper troposphere and lower stratosphere.

Table 3.1: Recently supported scientific campaigns at Esrange.

Campaign	Platform	Year	Aim of the support
BEXUS	balloon	2008, 2009	stratospheric background
REXUS	rocket	2009, 2010	mesospheric temperature
RECONCILE	aircraft	2010	PSCs
CNES campaign	balloon	2011	PSCs and temperature
PHOCUS	rocket	2011	Noctilucent clouds
in-situ IWC	balloon	2013	cirrus, aerosol extinction, and temperature

Further, the new setup makes the Esrange lidar a relied instrument/tool for monitoring launch conditions for rockets and balloons and for guiding launch–related decision making. Recent scientific campaigns that relayed on Esrange lidar observations for selecting appropriate launch conditions are presented in Table 3.1. Lidar measurements of Nuctilucent Clouds (mesospheric clouds) in the morning of 21 July 2011 allowed for a successful launch of the PHOCUS (Particles, Hydrogen and Oxygen Chemistry in the Upper Summer mesosphere) rocket experiment. The aim of the PHOCUS measurement was to conduct measurements within a Nuctilucent cloud. On the 19th and 20th of February 2013 the Esrange lidar and balloon–borne in–situ instrument conducted combined measurements of the volume extinction coefficient and the ice water content of ice clouds, respectively. The aim of the balloon launches was to determine the relationship between ice water content and volume extinction coefficient of thin ice–clouds (cirrus) and to setup a database of the size, shape, volume, as well as ambient temperature and humidity of ice clouds in the upper troposphere (Kuhn *et al.*, 2012). This will be a basis for the development of new cloud parameterizations for climate models.

4. CALIPSO Lidar Measurements and Findings

Space–borne lidar measurements can provide global observations of clouds and aerosols with high vertical and spatial resolution. The first space–borne lidars flew aboard the space shuttle Discovery and the MIR space station. The Lidar In-space Technology Experiment (LITE) aboard Discovery was launched for a 10–day mission in September 1994 (McCormick, 2005). LITE was a three–wavelengths lidar (355, 532, and 1064 nm) and the conducted measurements of Sahara dust layers, biomass burning smoke, and pollution outflow from the continents showed the potential for long–duration space–borne lidar missions. Further, LITE showed that space–borne lidars could provide near–surface information for 60% of the total measurement period (Winker *et al.*, 1996). However, it should take more than a decade until the first long–duration mission of a space–borne lidar became reality.

4.1 The CALIPSO Lidar

The space–borne Cloud–Aerosol Lidar with Orthogonal Polarization (CALIOP) aboard the Cloud–Aerosol Lidar and Infrared Pathfinder Satellite Observations (CALIPSO) satellite is the first long–duration space–borne lidar. CALIOP is a two-wavelength (532 and 1064 nm) lidar and operates from a polar near–earth orbit at about 700 km height. It was designed to provide global and vertically–resolved measurements of clouds and aerosols to improve our understanding of their role in the climate system (Winker *et al.*, 2003). The CALIPSO satellite is part of the NASA/ESA A–Train satellite constellation and is in orbit since April 2006. Although PSC observations are not one of its primary missions CALIPSO is an ideal platform for such studies. CALIOP represents a perfect tool to provide a vortex–wide perspective of PSCs (Pitts *et al.*, 2009, 2011). CALIPSO provides a high measurement coverage over both polar regions with an average of 14 orbits per day. About 300000 daily lidar profiles are acquired between 55 and 82° N, and form a unique dataset for studying the occurrence, composition, and evolution of Arctic PSCs (Pitts *et al.*, 2007). CALIPSO profiles are generated on a non–uniform altitude and time grid (Winker *et al.*,

2007) and are available at http://www-calipso.larc.nasa.gov/products/. The vertical resolution of the CALIPSO profiles varies with altitude from 30 m below 8.5 km height, 60 m between 8.5 and 20.1 km height, and 180 m between 20.1 and 30.1 km height.

4.2 CALIPSO Measurement of PSCs

In contrast to ground–based lidar measurements CALIPSO observations do not rely on cloud–free conditions in the troposphere. The downward–looking configuration allows for simultaneous observations of tropospheric clouds and PSCs. Wang *et al.* (2008) used CALIPSO observations to study the concurrent occurrence of PSCs and tropospheric clouds over Antarctica. Further, Adhikari *et al.* (2010) showed that high and deep–tropospheric cloud systems have a significant effect on the relative occurrence of different PSC types over the Antarctic — especially on ice PSCs. They showed that during the period June–October 2006 66% and 52% of the PSCs over western and eastern Antarctica, respectively, were associated with an underlying deep-tropospheric cloud system. In Paper III of this thesis we used observations from CALIPSO between December 2007 and February 2008 to study the possible relationship between the occurrence of Arctic PSCs and tropospheric clouds. CALIPSO PSC observations were classified according to the underlying tropospheric clouds to investigate their influence on PSC microphysical properties. For classification of the three PSC types we utilize the combination of the linear aerosol depolarization ratio (δ_{aer}) and the total backscatter ratio (R^{T}) as was done by Adriani *et al.* (2004) and Massoli *et al.* (2006).

Between 15 December 2007 and 6 February 2008 a total number of 211 PSCs were identified in the CALIPSO lidar observations over the Arctic. A time–resolved display of these observations is given in Figure 4.1a. The identified PSCs were analyzed with respect to their composition (Figure 4.1b) and the type of underlying tropospheric clouds. The highest number of PSCs was observed in early January 2008. Mixed–phase (47%) and type Ib (STS) PSCs (37%) dominated during the period under investigation. Ice PSCs (11%) were rarely observed during that winter. NAT PSCs (5%) were mainly observed during January while February was dominated by pure STS clouds.

All 211 PSCs observed during CALIPSO overpasses during the winter 2007/2008 were classified and sorted into four different groups with respect to the underlying tropospheric cloud systems. 172 of the 211 PSC observations (81.5% of all PSCs) occurred in connection with tropospheric clouds. 72% of these 172 PSCs (58.8% of all PSCs) were observed over deep-tropospheric cloud systems. 26 cases of PSCs were found over mid-tropospheric clouds (12.3% of all cases) while 22 cases of PSCs were oberved over cirrus (10.4%

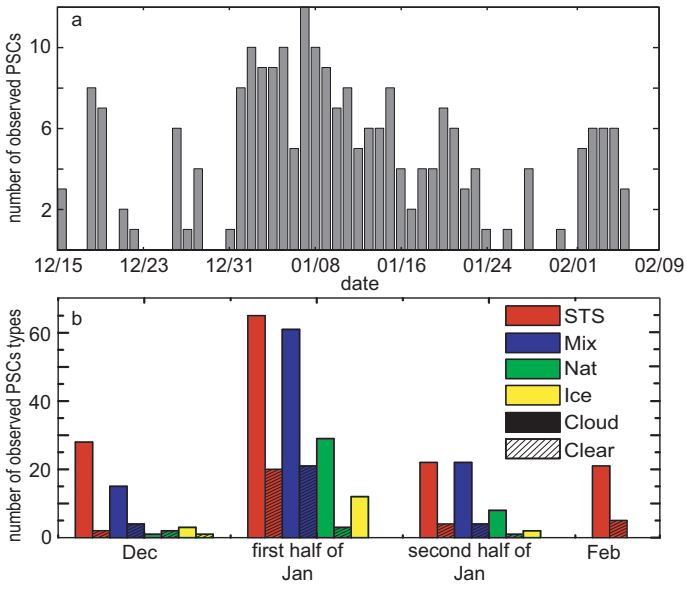

Figure 4.1: (a) Daily resolved number of PSCs detected in CALIPSO measurements north of 60° N during winter 2007/2008. (b) Analysis of the PSC observations in accordance to their type. Unshaded and shaded bars refer to observations over tropospheric clouds or during the absence of tropospheric clouds, respectively. The distribution differs from the display in (a) because individual PSCs might contain areas of different composition.

of all cases). The remaining 39 PSCs (18.5% of all cases) showed an absence of underlying tropospheric clouds. For comparison a deep tropospheric cloud without a PSC above occurred during 28% of the observations. During the entire period ice PSCs were only once observed during the absence of tropospheric clouds (Figure 4.1b, shaded area). The findings of Paper 3 revealed a similar result for Arctic PSCs compared to what was presented in previous studies of Antarctic PSCs by Wang *et al.* (2008) and Adhikari *et al.* (2010). Furthermore, the findings of Paper III indicate that the tropospheric control of PSC occurence is governed by adiabatic cooling connected to mesoscale cyclonic dynamics rather than by radiative cooling. Though the study presented in this thesis is restricted to one Arctic winter a clear connection between tropospheric clouds and PSC occurrence could be established. Future studies which consider the entire CALIPSO data set (six Arctic winters so far) would be very valuable to provide insight into the processes behind the observed connection.

4.3 Combined Space–borne and Ground–based Lidar Measurements

In order to investigate PSC formation, cloud microphysics, and the history of the PSC air parcel need to be quantified. The microphysical properties can be determined from lidar measurements. The history of the PSC parcels can be determined from meteorology data (e.g., back–trajectory analysis) and microphysical model simulations. In Paper IV of this thesis ground–based and space–borne lidar measurements were combined with microphysical box–model simulations along 72–h backward trajectories to gain new insight into PSC formation.

The case study discussed in Paper IV focuses on a PSC observation between 18 and 26 km on 22 and 23 January 2008. 72–h back trajectories based on ECMWF analyses were calculated between 72 hPa (16 km height) and 11 hPa (27 km height) in steps of 1 km to investigate the connection between PSCs that were observed over Esrange and by the CALIPSO lidar. The backward trajectories shown in Figure 4.2 were started at 0000 UT (left) and 0600 UT (right) on the 23rd January 2008. The PSC over Esrange was classified according to the method described in Blum *et al.* (2005b). At 0000 UT the PSC consisted of STS particles between 21 and 25 km and a mixed–layer at cloud base. AT 0600 UT the PSC consisted of a STS layer between 20 and

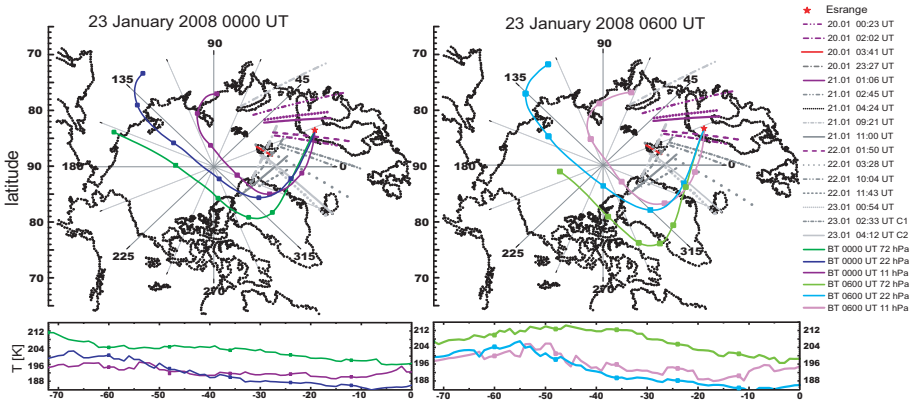

Figure 4.2: 72–h backward trajectories ending at 72 hPa (green), 22 hPa (blue), and 11 hPa (purple) height level over Esrange on 23 January 2008 at 0000 UT (left) and 0600 UT (right). CALIPSO observations within 72 h before the observation at Esrange are shown as well. Type Ia PSCs are shown as purple lines and type Ib PSCs are shown as gray lines. The temperature along the backward trajectories are shown in the bottom panel.

24 km and a NAT layer between 24 and 26 km.

The temperature along the trajectory (Figure 4.2, bottom panel) at the 72–hPa and 11–hPa levels was found to be too warm for PSC formation. At all other altitude levels NAT existence temperature was achieved before the air mass reached Esrange. At the 22–hPa level (23 km) NAT existence temperature was reached between 40 to 38 h before the observation with the ground–based lidar system at Esrange. CALIPSO observed two PSCs along the air parcel back trajectory: one around 0240 UT and a second one around 0420 UT on 23 January 2008. The aerosol depolarization ratio was around zero for both measurements. Thus, the PSCs consisted mainly of STS (type Ib). Several widespread PSCs with different composition were observed by CALIPSO between Greenland and Norway in the time period from 20 to 23 January 2008. All these PSCs were identified as type Ib (Figure 4.2, gray lines). In the same time period CALIPSO observed type Ia PSCs over Scandinavia (Figure 4.2, purple lines). The PSCs observed by CALIPSO were classified according to the method described in Massoli *et al.* (2006).

Box model studies (Blum *et al.*, 2006) revealed that the PSC that was identified over Esrange formed about 20 h prior to its observation. At this time the air mass was located over Greenland. The composition of the PSC changed from STS to a mixed–phase PSC within the moving air mass. A likely scenario is that the solid particles started to form when the air mass reached the Scandinavian mountains about 4 h prior to the observations at Esrange. This is in agreement with the CALIPSO observations.

5. Outlook

This thesis focused on the observation and classification of PSCs in the Arctic by means of ground–based lidar measurements at Esrange and space–borne lidar measurements. In order to improve our understanding of the processes that govern PSC formation (in particular that of type Ia PSCs) sophisticated PSC characterization needs to be combined with a detailed view on the atmospheric background conditions in which individual PSCs develop, exist, and are transformed from one type to another.

As outlined in Section 3.1 and described in detail in Paper I, a key aspect of this work was to upgrade the Esrange lidar to keep it a state–of–the–art tool for PSC observations. The instrument not only allows for a detailed characterization of PSC microphysical properties. It is also capable of measuring ambient temperature within PSCs. The formation of different PSCs types depends strongly on temperature. Note that PSC studies generally rely on temperature information from models and that concurrent temperature measurements are rare.

The new detection setup of the Esrange lidar and its growing data set of PSC observations provide the foundation for future PSC studies that will help to improve our understanding of PSC formation. These studies benefit from the geographical location of Esrange in the lee of the Scandinavian mountain range, where mountain–wave activity triggers the formation of a wide range of PSC types and subtypes. Furthermore, the developments with focus on atmospheric temperatures, volume–extinction–coefficient measurements, and an improved characterization of cloud and aerosol particles are important to support future balloon campaigns studying PSCs processes.

Space–borne lidar observations provide an unprecedented opportunity for studying the connection between PSCs and underlying synoptic–scale conditions that manifest, e.g., as tropospheric clouds. Section 4.2 and Paper III presented first insights on this connection. The growing size of the CALIPSO data set will form a foundation for future studies of PSC–tropospheric–clouds connections. The CALIPSO data set also forms the first polar–wide time series of PSC observations that is not biased to tropospheric conditions (cloud cover). Hence, a completely new perspective on PSCs and related processes is offered by space–borne observations.

From a combination of ground–based and space–borne lidar measurements

with microphysical modeling it is possible to reconstruct the evolution of an individual PSC and the formation of different PSC types (see Section 4.3 and Paper IV). The box model that was applied for describing the processes within PSCs is only suitable for the parameterization of PSC of type Ib. For future studies microphysical models that are capable of describing the three main PSC types should be used. New insight in PSC–related processes will be obtained in the future when such improved models are combined with the meteorological information along trajectories that describe the movement of the observed air parcel.

Different classification schemes for PSC characterization with lidar are reported in the literature. Within the different classification schemes varying thresholds are used to separate between PSC types. As discussed in Section 3.4 and Paper II a wide spread is found in occurrence of different PSC types when applying several classification schemes to the 17–year time series of Esrange lidar measurements. A homogenization of lidar–based classification schemes seems to be necessary for a reliable and comparable interpretation of PSC observations in the future. Since lidar has been used since decades for PSC measurements a unified view of various lidar statistics could be used to gain more inside into the occurrence of different PSC types and the accompanying atmospheric conditions.

Acknowledgements

First and foremost, I would like to thank my supervisor Farahnaz Khosrawi and my co-supervisor Jörg Gumbel for giving me the opportunity to study at MISU, for sharing their expertise in the field, and for giving me the opportunity to work with the Esrange lidar.

I am particularly thankful to K. H. Fricke for teaching me everything about the Esrange lidar, for the long and interesting scientific discussions at Esrange, and all the help to get started with the thesis. Also many thanks to Ulrich Blum for all the support during my thesis.

For all the support during my stays at Esrange I would like to thank the Esrange personnel. Special thanks go to Marko, Mette, Stig, and Thord. Especially the conversations with Thord have loosened the workday. But I am still waiting for the cake! I would like to thank Peter Voelger of IRF for all the long calls and scientific discussions during the night shifts with the lidar. Many thanks go to Misha for helping me to upgrade the lidar and to get the measurements going. Thanks also to Stefan, Jonas, and Kristoffer for helping with the measurements. One day I will win a billiard game against you!

Many thanks go to my officemate Abubakr for all the interesting conversations and for taking care of my plants when I was on a campaign. Keep on your business plans. We could be rich, if I had listened to your idea of collecting a little fee for our candy and the support for *tuba*. I would like to thank L. P. and Matze for not spoiling *Game of Thrones* for me by kindly kicking me out of my office for their discussions. I hope book 6 will be out soon! Thanks to everyone who participated in the weekly badminton match and the crowd who joined for the Green Villa on Thursday. And yes, we earned those beers! Thanks go to, Susanne, Gao, Qiong, Anna, Raza, Saeed, Mondheur, Linda, Bodil, John, Marie, Wing, Cian, and Friederike who made MISU to a fun place to work at. To Anders thanks for his help with burning up the sugar loaf for the yearly *Feuerzangenbowle*. I would like to thank Jan for his compliment: “Why do you Germans not behave like the Germans in an American sitcom?”

Last but not least I want to thank my family for their support during the last years. Danke Jens, dass du so oft auf der Matte standest. Finally, I would like to thank Matthias for finishing his thesis and joining me in Stockholm. Aber wie immer hatte ich recht: man kann es auch in kürzerer Zeit schaffen!

References

ADHIKARI, L., WANG, Z. & LIU, D. (2010). Microphysical properties of Antarctic Polar Stratospheric Clouds and their dependence on tropospheric cloud systems. *J. Geophys. Res.*, **115**. 13, 30, 31

ADRIANI, A., MASSOLI, P., DI DONFRANCESCO, G., CAIRO, F., MORICONI, M. & SNELS, M. (2004). Climatology of Polar Stratospheric Clouds based on lidar observations from 1993 to 2001 over McMurdo Station, Antarctica. *J. Geophys. Res.*, **109**. 25, 30

BEHRENDT, A. (2005). *Temperature Measurements with Lidar, in LIDAR: Range–Resolved Optical Remote Sensing of the Atmosphere*. Springer. 22, 23

BIELE, J., TSIAS, A., LUO, B.P., CARSLAW, K.S., NEUBER, R., BEYERLE, G. & PETER, T. (2001). Non–equilibrium coexistence of solid and liquid particles in Arctic stratospheric clouds. *J. Geophys. Res.*, **106**, 991–23. 22, 25

BLUM, U. & FRICKE, K.H. (2005a). The Bonn University lidar at the Esrange: Technical description and capabilities for atmospheric research. *Ann. Geophys.*, **23**, 1645–1658. 17, 18, 22

BLUM, U., FRICKE, K.H., MÜLLER, K.P., SIEBERT, J. & BAUMGARTEN, G. (2005b). Long–term lidar observations of Polar Stratospheric Clouds at Esrange in northern Sweden. *Tellus*, **57B**, 412–422. 25, 26, 27, 32

BLUM, U., KHOSRAWI, F., BAUMGARTEN, G., STEBEL, K., MÜLLER, R. & FRICKE, K.H. (2006). Simultaneous lidar observations of a Polar Stratospheric Cloud on the east and west sides of the Scandinavian Mountains and microphysical box model simulations. *Ann. Geophys.*, **24**, 3267–3277. 33

BROWELL, E.V., BUTLER, C.E., ISMAIL, S., ROBINETTE, P.A., CARTER, A.F., HIGDON, N.S., TOON, O.B., SCHOEBERL, M.R. & TUCK, A.F. (1990). Airborne lidar observations in the wintertime Arctic stratosphere: Polar Stratospheric Clouds. *Geophys. Res. Lett.*, **17**, 385–388. 13, 24

CARSLAW, K.S., LUO, B.P., CLEGG, S.L., PETER, T., BRIMBLECOMBE, P. & CRUTZEN, P.J. (1994). Stratospheric aerosol growth and HNO3 gas phase depletion from coupled HNO3 and water uptake by liquid particles. *Geophys. Res. Lett.*, **21**, 2479–2482. 13, 24

CARSLAW, K.S., WIRTH, M., TSIAS, A., LUO, B.P., DÖRNBRACK, A., LEUTBECHER, M., VOLKERT, H., RENGER, W., BACMEISTER, J.T., REIMERS, E. & PETER, T.H. (1998). Increased stratospheric ozone depletion due to mountain-induced atmospheric waves. *Nature*, **391**, 675–678. 13

CRUTZEN, P.J. (1979). The role of NO and NO2 in the chemistry of the troposphere and stratosphere. *Ann. Rev. Earth and Planet. Sci.*, **7**, 443–472. 15

DAVID, C., BEKKI, S., GODIN, S., MEGIE, G. & CHIPPERFIELD, M.P. (1998). Polar Stratospheric Clouds climatology over Dumont d'Urville between 1989 and 1993 and the influence of volcanic aerosols on their formation. *J. Geophys. Res*, **103(D17)**, 22163–22180. 24

DÖRNBRACK, A., LEUTBECHER, M., BEHREND, J.R.A., MÜLLER, K.P. & BAUMGARTEN, G. (2000). Relevance of mountain wave cooling for the formation of polar stratospheric clouds over Scandinavia: Mesoscale dynamics and observations for January 1997. *J. Geophys. Res.*, **106(D2)**, 1569–1581. 13

FADUILHE, D., KECKHUT, P., BENCHERIF, H., ROBERT, L. & BALDY, S. (2005). Stratospheric temperature monitoring using a vibrational Raman lidar, Part 1: Aerosols and ozone interferences. *J. Environ. Monitor*, **7**, 357–364. 22

FAHEY, D.W., GAO, R.S., CARSLAW, K.S., KETTLEBOROUGH, J., POPP, P.J., NORTHWAY, M.J., HOLECEK, J.C., CICIORA, S.C., MCLAUGHLIN, R.J., THOMPSON, T.L. & ET AL. (2001). The detection of large HNO3–containing particles in the winter Arctic stratosphere. *Science*, **291**, 1026–1031. 25

GUMBEL, J. (2007). Atmospheric science with sounding rockets–present status and future perspectives. In *Proc. 18th ESA Symposium on European Rocket and Balloon Programmes and Related Research*, ESA SP-647, 47–54. 27

HALLETT, J. & LEWIS, R.E.J. (1967). Mother–of–pearl clouds. *Weather*, **22**, 56–65. 9

HAUCHECORNE, A., CHANIN, M.L., KECKHUT, P. & NEDELJKOVIC, D. (1992). LIDAR monitoring of the temperature in the middle and lower atmosphere. *Appl. Phys. B*, **55**, 29–34. 22

HILDEBRANDSON, H., RIGGENBACH, A. & DE BORT, L. (1896). *International Cloud–Atlas*. World Meteorological Organization. 11

HOLTON, J.R. (1992). *An Introduction to Dynamic Meteorology*. Academic Press., Inc. 14

HÖPFNER, M., BLUMENSTOCK, T., HASE, F., ZIMMERMANN, A., FLENTJE, H. & FUEGLISTALER, S. (2001). Mountain polar stratospheric cloud measurements by ground based FTIR solar absorption spectroscopy. *Geophys. Res. Lett.*, **28**, 2189–2192. 13

HÖPFNER, M., LARSEN, N., SPANG, R., LUO, B.P., MA, J., SVENDSEN, S.H., ECKERMANN, S.D., KNUDSEN, B., MASSOLI, P., CAIRO, F., STILLER, G., CLARMANN, T. & FISCHER, H. (2006). MIPAS detects Antarctic stratospheric belt of NAT PSCs caused by mountain waves. *Atmos. Chem. Phys.*, **6**, 1221–1230. 13

JUÁREZ, M.D., MARCUS, S., DÖRNBRACK, A., SCHRØDER, T.M., KIVI, P., IIJIMA, B.A., HAJJ, G.A. & MANNUCCI, A.J. (2009). Detection of temperatures conducive to Arctic Polar Stratospheric clouds using CHAMP and SAC–C radio occultation data. *J. Geophys. Res.*, **114**. 13

KECKHUT, P., CHANIN, M.L. & HAUCHECORNE, A. (1990). Stratosphere temperature measurement using Raman lidar. *Appl. Optics*, **29**, 5182–5186. 22

KUHN, T., HEYMSFIELD, A.J. & BUEHLER, S.A. (2012). In–situ ice particle measurements over northern Sweden. In *Geophysical Research Abstracts*, vol. 14. 28

LABITZKE, K. & LOON, H. (1999). *The Stratosphere*. Springer. 14

MASSOLI, P., MATURILLI, M. & NEUBER, R. (2006). Climatology of Arctic Polar Stratospheric Clouds as measured by lidar in Ny–Ålesund, Spitsbergen (79° N, 12° E). *J. Geophys. Res.*, **111(D9)**. 25, 30, 33

MCCORMICK, M.P. (2005). *Airborne and Spaceborne Lidar, in LIDAR: Range–Resolved Optical Remote Sensing of the Atmosphere*. Springer. 29

MCCORMICK, M.P., HAMILL, P., PEPIN, T.J., CHU, W.P., SWISSLER, T.J. & MCMASTER, L.R. (1982). Satellite studies of the stratospheric aerosol. *Bull. Am. Meteorol. Soc.*, **60**, 1038–1046. 9, 24

MCDONALD, A.J., GEORGE, S.E. & WOOLLANDS, R.M. (2009). Can gravity waves significantly impact PSC occurrence in the Antarctic? *Atmos. Chem. Phys.*, **9(22)**, 8825–8840. 13

MOHN, H. (1893). Irisirende Wolken. *Meteorol. Zeitung*, **10**, 81–97. 11

PITTS, M.C., THOMASON, L.W., POOLE, L.R. & WINKER, D.W. (2007). Characterization of Polar Stratospheric Clouds with spaceborne lidar: CALIPSO and the 2006 Antarctic season. *Atmos. Chem. Phys.*, **7**, 5207–5228. 29

PITTS, M.C., POOLE, L.R. & THOMASON, L.W. (2009). CALIPSO Polar Stratospheric Cloud observations: Second–generation detection algorithm and composition discrimination. *Atmos. Chem. Phys.*, **9**, 7577–7589. 29

PITTS, M.C., POOLE, L.R., DÖRNBRACK, A. & THOMASON, L.W. (2011). The 2009/2010 Arctic Polar Stratospheric Cloud season: A calipso perspective. *Atmos. Chem. Phys.*, **11**, 2161–2177. 29

POOLE, L.R. & MCCORMICK, M.P. (1988). Airborne lidar observations of Arctic Polar Stratospheric Clouds: Indication of two distinct growth stages. *Geophys. Res. Lett.*, **15**, 21–23. 9, 24

SANTACESARIA, V., MACKENZIE, A.R. & STEFANUTTI, L. (2001). A climatological study of Polar Stratospheric Cloud (1989–1997) from LIDAR measurements over Dumont d'Urville (Antarctica). *Tellus*, **53B**, 306–321. 25

SEINFELD, J.H. & PANDIS, S.N. (2006). *Atmospheric chemistry and physics*. Wiley. 15, 16

SHIBATA, T., SHIRAISHI, K., ADACHI, H., IWASAKA, Y. & FUJIWARA, M. (1999). On the lidar–observed sandwich structure of Polar Stratospheric Cloud (PSCs): 1. Implications for the mixing state of the PSC particles. *J. Geophys. Res.*, **104**, 603–621. 25

STANFORD, J.L. & DAVIS, J.S. (1974). A century of stratospheric cloud reports. *Bull. Am. Meteorol. Soc.*, **55**, 213–219. 9

STEELE, H.M., HAMILLP, P., MCCORMICK, M.P. & SWISSLER, T.J. (1983). The formation of Polar Stratospheric Clouds. *J. of Atmos. Science*, **40(8)**, 2055–2067. 9

STEIN, B., WEDEKIND, C., WILLE, H., IMMLER, F., MÜLLER, M., WÖSTE, L., DEL GUASTA, M., MORANDI, M., STEFANUTTI, L., ANTONELLI, A. & ET AL. (1999). Optical classification, existence temperatures, and coexistence of different polar stratospheric cloud types. *J. Geophys. Res.*, **104**, 23983–23993. 25

STÖRMER, C. (1929). Remarkable clouds at high altitudes. *Nature*, **123**, 260–261. 12

STÖRMER, C. (1931). Höhe und Farbenverteilung der Perlmutterwolken. *Geof. Publ.*, **IX**, 3–27. 12

TEITELBAUM, H., MOUSTAOUI, M. & FROMM, M. (2001). Exploring polar stratospheric cloud and ozone minihole formation: The primary importance of synoptic–scale flow perturbations. *J. Geophys. Res.*, **106**, 28173–28188. 13

TOON, O.B., BROWELL, E.V., KINNE, S. & JORDAN, J. (1990). An analysis of lidar observations of Polar Stratospheric Clouds. *Geophys. Res. Lett.*, **17**, 393–396. 13, 24

TOON, O.B., TABAZADEH, A., BROWELL, E.V. & JORDAN, J. (2000). Analysis of lidar observations of Arctic Polar Stratospheric Cloud during January 1989. *J. Geophys. Res.*, **105(D16)**, 20589–20615. 25

TSIAS, A., WIRTH, M., CARSLAW, K.S., BIELE, J., MEHRTENS, H., REICHARDT, J., WEDEKIND, C., WEISS, V., RENGER, W., NEUBER, R. & ET AL. (1999). Aircraft lidar observations of an enhanced type Ia polar stratospheric clouds during APE–POLECAT. *J. Geophys. Res.*, **104(D19)**. 25

VOIGT, C., SCHLAGER, H., LUO, B.P., DÖRNBRACK, A., ROIGER, A., STOCK, P., CURTIUS, J., VÖSSING, H., BORRMAN, S., DAVIES, S., KONOPKA, P., SCHILLER, C., SHUR, G., & PETER, T. (2005). Nitric acid trihydrate (NAT) formation at low NAT supersaturation in polar stratospheric clouds (PSC). *Atmos. Chem. Phys.*, **5**, 1371–1380. 13, 24

VON HOBE, M., BEKKI, S., BORRMANN, S., CAIRO, F., D'AMATO, F., DONFRANCESCO, G.D., ÖRNBRACK, A., EBERSOLDT, A., EBERT, M., EMDE, C. & ET AL. (2012). Reconciliation of essential process parameters for an enhanced predictability of arctic stratospheric ozone loss and its climate interactions. *Atmos. Chem. Phys. Discuss.*, **12**, 30661–30754. 27

WANDINGER, U. (2005). *Introduction to Lidar, in LIDAR: Range–Resolved Optical Remote Sensing of the Atmosphere*. Springer. 17

WANG, Z., STEPHENS, G., DESHLER, T., TREPTE, C., PARISH, T., VANE, D., WINKER, D., LIU, D. & ADHIKARI, L. (2008). Association of Antarctic Polar Stratospheric Cloud formation on tropospheric cloud systems. *J. Geophys. Res.*, **35**. 13, 30, 31

WINKER, D.M., COUCH, R.H. & MCCORMICK, M.P. (1996). An overview of LITE: NASA's Lidar In-space Technology Experiment. In *Proc. IEEE*, vol. 84, 164–180. 29

WINKER, D.M., PELON, J. & MCCORMICK, M.P. (2003). The CALIPSO mission: Spaceborne lidar for observation of aerosols and clouds. In *Proc. SPIE*, 4893, 1–11. 29

WINKER, D.M., HUNT, W.H. & MATTHEW, J.M. (2007). Initial performance assessment of CALIOP. *Geophys. Res. Lett.*, **34**. 29